

Observation of Néel-type skyrmions in acentric self-intercalated $\text{Cr}_{1+\delta}\text{Te}_2$

Rana Saha ¹, Holger L. Meyerheim¹, Börge Göbel ², Binoy Krishna Hazra ¹, Hakan Deniz¹, Katayoon Mohseni¹, Victor Antonov³, Arthur Ernst ^{1,4}, Dmitry Knyazev¹, Amilcar Bedoya-Pinto ^{1,5}, Ingrid Mertig² & Stuart S. P. Parkin ¹✉

Transition-metal dichalcogenides intercalated with 3d-transition metals within the van der Waals (vdW) gaps have been the focus of intense investigations owing to their fascinating structural and magnetic properties. At certain concentrations the intercalated atoms form ordered superstructures that exhibit ferromagnetic or anti-ferromagnetic ordering. Here we show that the self-intercalated compound $\text{Cr}_{1+\delta}\text{Te}_2$ with $\delta \approx 0.3$ exhibits a new, so far unseen, three-dimensionally ordered ($2 \times 2 \times 2$) superstructure. Furthermore, high resolution X-ray diffraction reveals that there is an asymmetric occupation of the two inequivalent vdW gaps in the unit cell. The structure thus lacks inversion symmetry, which, thereby, allows for chiral non-collinear magnetic nanostructures. Indeed, Néel-type skyrmions are directly observed using Lorentz transmission electron microscopy. The skyrmions are stable within the accessible temperature range (100–200 K) as well as in zero magnetic field. The diameter of the Néel skyrmions increases with lamella thickness and varies with applied magnetic field, indicating the role of long-range dipole fields. Our studies show that self-intercalation in vdW materials is a novel route to the formation of synthetic non-collinear spin textures.

¹Max Planck Institute of Microstructure Physics, Weinberg 2, Halle (Saale) 06120, Germany. ²Institute of Physics, Martin Luther University, Halle-Wittenberg, Halle (Saale) 06120, Germany. ³G. V. Kurdyumov Institute for Metal Physics, National Academy of Science of Ukraine, 03142 Kiev, Ukraine. ⁴Institute for Theoretical Physics, Johannes Kepler University Linz, Altenberger Strasse 69, A-4040 Linz, Austria. ⁵Instituto de Ciencia Molecular, Universidad de Valencia, Catedrático José Beltrán 2, Paterna 46980, Spain. ✉email: stuart.parkin@mpi-halle.mpg.de

Within the group of magnetic and non-magnetic van der Waals (vdW) materials^{1,2}, transition metal dichalcogenides (TMDs) represent a unique class of materials due to their layered arrangements and structural flexibility, the latter related to their ability to intercalate atoms into the vdW gaps^{3–6}. Although vdW materials and TMDs have been studied for some time, more recently they have attracted intense interest owing to their remarkable magnetic properties in atomically thin layers^{7–10}. Of the large number of TMDs those which have been reported to exhibit magnetic long-range order include MnSe_x¹¹ and CrTe₂¹². For the latter, a considerable number of studies concerning the thickness-dependent magnetic properties have been carried out, albeit with a notable scatter in the results reported with regard to the thickness dependence of the Curie temperature, the easy axis of magnetization, as well as the concentration of intercalants^{13–18}. Most importantly, in all these previous reports the crystal structures in all thickness regimes were assumed to be highly symmetric belonging to the space group (SGR) $P\bar{3}m$, which is inversion symmetric. Inversion symmetry rules out many important physical properties which are related to polar tensors of odd rank and axial tensors of even rank¹⁹. In particular, the latter is related to the stabilization of non-collinear magnetism where the Dzyaloshinskii-Moriya interaction (DMI)^{20–22} plays a decisive role. The DMI competes with the Heisenberg exchange interaction to stabilize various types of chiral magnetic textures in non-centrosymmetric magnetic materials^{23–27}. Only very recently has it been observed that massive structural relaxations in TMDs are present in the two-dimensional (2D) limit. For example, in a single TaSe₂ monolayer, which is otherwise non-magnetic, a reduction in symmetry gives rise to the appearance of chiral magnetic states²⁸.

Here we show that in a bulk Cr_{1+ δ} Te₂ ($\delta \approx 0.3$) single crystal the prior assumption of an inversion symmetric structure is not correct and, as a consequence, a non-collinear chiral magnetic texture in the form of Néel-type skyrmions appears. While in the past only two-dimensional superstructures of type (2 \times 2) and ($\sqrt{3}\times\sqrt{3}$) were reported for ordered intercalated structures, here we observe a new, so far unknown three-dimensional (2 \times 2 \times 2) superstructure. It is characterized by the existence of two inequivalent vdW gaps, both partially filled by Cr atoms. As a consequence, the neighboring Te-Cr-Te triple layers (TLs) experience an asymmetric environment involving relaxations of the atomic positions along the vertical c -axis, thereby reducing the crystal symmetry from $P\bar{3}m$ to $P3m1$, the latter being acentric. The latter has a C_{3v} point group that is compatible with the appearance of Néel-type magnetic textures, which we directly observe by Lorentz transmission electron microscopy (LTEM). Our results point to a new approach to stabilize non-collinear spin textures via self-intercalation in vdW magnets, which is distinct from schemes that make use of heteroepitaxial systems to induce skyrmions in vdW magnetic materials^{29,30}.

Results and discussion

Single crystals of Cr_{1+ δ} Te₂ were grown by the flux zone growth method³¹. The structural and magnetic properties of the crystals were characterized by X-ray diffraction (XRD) and SQUID magnetometry, respectively. At room-temperature bulk CrTe₂ was previously reported to crystallize in a trigonal structure with the centrosymmetric SGR $P\bar{3}m$ ³².

In the following, we discuss XRD experiments carried out at room temperature, where a plate-like single crystal was investigated by collecting 158 symmetry independent reflections whose squared structure factor magnitudes ($|F_{\text{obs}}(\text{HKL})|^2$) span five orders of magnitude. In total, 36 reflections have integer HKL values, with respect to the trigonal unit cell whose lattice parameters ($a = b = 3.91 \text{ \AA}$, $c = 5.99 \text{ \AA}$) are close to those previously

reported of $a = 3.92 \text{ \AA}$ and $c = 6.02 \text{ \AA}$, respectively³². Figure 1a shows a line scan along the reciprocal b^* axis at $L = 1$ reciprocal lattice units, i.e. reflections of type (0 K 1) for K varying between 0.2 and 3.7. We also observe reflections of type H = K = L = $(2n + 1)/2$, with n equal to an integer as shown in Fig. 1b, which, in combination with the three-fold symmetry of the diffraction pattern, is an unambiguous proof for the presence of a (2 \times 2 \times 2) superstructure [see also Supplementary Information (SI)]. The low intensity of the half order reflections arise from the fact that they originate from the difference between the Cr-intercalation structures in the two vdW gaps. At the half-order reflections there is an anti-phase relation between the waves scattered by the Cr atoms residing in the different vdW gaps. Therefore, they also show a strongly suppressed temperature dependence, as outlined in the Supplementary Information (SI). The half-order reflections are several orders of magnitude lower in intensity than the integer-order reflections.

In a least squares structural refinement which takes only the (1 \times 1 \times 1) integer order reflections into account the previously reported structural model is accurately reproduced in which the symmetry corresponds to the centrosymmetric SGR $P\bar{3}m$ (SGR#164)^{32,33}. Here, Te atoms are located at the Wyckoff site $2d$ at $(x, y, z) = (1/2, 2/3, z)$ with $z = 0.248 \pm 0.001$ and Cr atoms are located at the site $1b$ (0 0 $\frac{1}{2}$). We obtain a good unweighted residuum (Ru)³⁴ of 0.064 and a goodness of fit (GOF)³⁵ near 1.0 provided that a fraction of 0.40 ± 0.10 atoms per unit cell of intercalated Cr is located in the vdW gap at the Wyckoff site $1a$ (0,0,0). On the basis of this structural model no significant improvement of the fit quality factors can be achieved by allowing for symmetry lowering such as e.g. by mapping the structure to the non-centrosymmetric SGR $P3m1$ (#156) and relaxing the z -positions of Te and Cr.

The presence of the half-order reflections along all three directions in reciprocal space directly indicates that the structure is considerably more complex. In Fig. 1c, d we show two sections ($y = 0$ and $y = 1/2$) of the charge density $[\rho(x, y, z)]$ within the ac plane. The charge density is the Fourier-Transform (FT) of the observed structure factors $[F_{\text{obs}}(\text{HKL})]$. Only the preliminary structural model including two Te-Cr-Te triple layers (TLs) was considered as input for the calculation of the scattering phases. Thus, $\rho(x, y, z)$ provides direct and quasi model-free evidence that the two vdW gaps (labeled by vdW(1) and vdW(2) in Fig. 1e) within the (2 \times 2 \times 2) unit cell are not equivalent. Charge densities (solid lines) in Fig. 1c, d are labeled by numbers for section ($y = 0$) and capital letters for section ($y = 1/2$). They relate to the correspondingly labeled atoms in the structural model shown in Fig. 1e. The most important result is that vdW(1) contains only one Cr atom at (0,0,0) (labeled by #1). By contrast, the intercalation in vdW(2) is characterized by three Cr sites, namely one position in section $y = 0$ at ($\frac{1}{2}, 0, \frac{1}{2}$), labeled by #8 and two positions in section $y = 1/2$ labeled by (#G) and (#H) at (0, $\frac{1}{2}, \frac{1}{2}$) and ($\frac{1}{2}, \frac{1}{2}, \frac{1}{2}$), respectively.

All these intercalated Cr atoms directly appear in $\rho(x, y, z)$. There are also several weaker peaks at asymmetric sites in $\rho(x, y, z)$, which, however, are related to truncation errors. The positions of the atoms and their occupancy factors were refined in a least-squares fit which confirms the structural model shown in Fig. 1e, as outlined in the SI. The two symmetrically inequivalent TLs adjacent to the vdW gaps experience an asymmetric environment which induces vertical relaxations of the atoms along z . These relaxations are primarily responsible for lowering the symmetry from the centrosymmetric SGR $P\bar{3}m$ to the non-centrosymmetric SGR $P3m1$. We emphasize that this model corresponds to the average structure within one domain which we estimate is $\sim 20 \text{ nm}$ in size. On a length scale smaller than the domain size the symmetry of the structure is likely to be reduced due to the statistical occupancy of

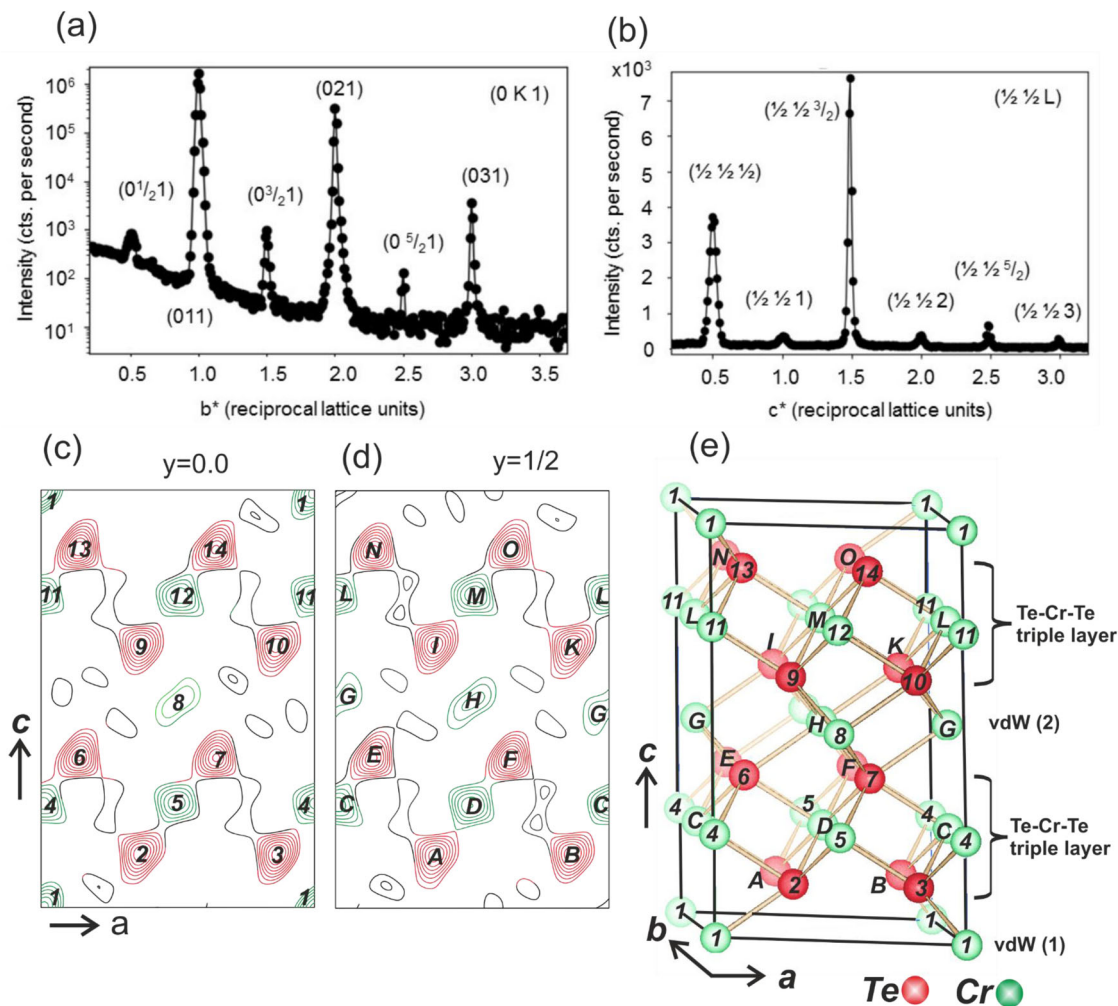


Fig. 1 Structural characterization of $\text{Cr}_{1+\delta}\text{Te}_2$ bulk crystal. **a** Line scan in reciprocal space along the b^* axis at $L=1$ crossing both integer and fractional order reflections of the $(2\times 2\times 2)$ $\text{Cr}_{1+\delta}\text{Te}_2$ bulk crystal. Reflections are labeled according to the $(1\times 1\times 1)$ unit cell. The intensity (counts per second) is shown on a logarithmic scale. Note, that the half order reflections are weaker than the integer order ones by several orders of magnitude. **b** Line scan along superlattice reflections of type $(\frac{1}{2}\frac{1}{2}L)$ between $L=0.2$ and 3.7 plotted on a linear scale. The observation of reflections with fractional indices along all three dimensions indicates the presence of a $(2\times 2\times 2)$ superstructure. **c-e** Charge density contour map of the $(2\times 2\times 2)$ $\text{Cr}_{1+\delta}\text{Te}_2$ structure calculated for sections $y=0$ (**c**) and $y=1/2$ (**d**) within the ac plane compared with the structural model (**e**). Cr (green) and Te (red) atoms in section $y=0$ and $y=1/2$ are labeled by numbers and capital letters, respectively. The van der Waals (vdW) gaps (1) and (2) are not equivalent inducing vertical atomic shifts within the adjacent Te-Cr-Te triple layers, thereby reducing the symmetry from the centrosymmetric space group $P\bar{3}m$ to the non-centrosymmetric space group $P3m1$.

the different vdW sites and the presence of vacancies. The presence of two different Cr environments, namely Cr atoms bound to Te atoms within the TLs and Cr atoms located within the vdW gaps, is also revealed by X-ray absorption experiments, where two distinct features are observed at the Cr $L_{2,3}$ absorption edge. In order to rule out multiplet splitting effects from a single Cr site³⁶, we have carried out *ab-initio* calculations of the Cr absorption spectra with and without Cr occupation in the vdW gaps. These calculations support our supposition that additional Cr atoms occupy the vdW gap sites, as discussed in the SI (Figs. S6, S10 and text). Also, our calculations of the spin-resolved electronic structure reveal that the presence of intercalated Cr atoms contributes to the formation of non-collinear spin structures.

Having assessed the presence of different Cr-sites, we proceed to characterize the magnetic properties of the crystal by magnetization measurements versus temperature and magnetic field, as shown in Fig. 2a, b. The temperature-dependent magnetization data, $M(T)$, (Fig. 2a) were recorded after field-cooling the crystal from 400 to 2 K in the presence of a out-of-plane $[0001]$ magnetic

field of 1, 10 and 70 kOe, which indicates that the crystal magnetically orders below 200 K (see Fig. S11 in the SI for the in-plane $M(T)$ data). Isothermal magnetization measurements as a function of magnetic field show a soft ferromagnetic hysteresis, as shown in Fig. 2b. From this figure we observe that at 2 K the $M(H)$ data saturate at a lower magnetic field when the field was applied along $[0001]$, whereas it does not saturate even if a magnetic field as large as 70 kOe is applied perpendicular to $[0001]$. The origin of such a large perpendicular anisotropy could be attributed to the presence of a high concentration of intercalated Cr atoms¹⁷ which is also supported by our calculations (see Figs. S8 and S9 and corresponding text in the SI). The lack of magnetic saturation when applying a large in-plane field has also been observed in element specific X-ray magnetic circular dichroism (XMCD) measurements at the Cr $L_{2,3}$ edge of a freshly cleaved $\text{Cr}_{1+\delta}\text{Te}_2$ crystal (Fig. S5 in SI). This indicates that the magnetic easy axis of the crystal is along the c -axis of the crystal. In the inset of Fig. 2b, a magnified region of the out of plane $M(H)$ loop is shown, characterized by a finite coercive field of

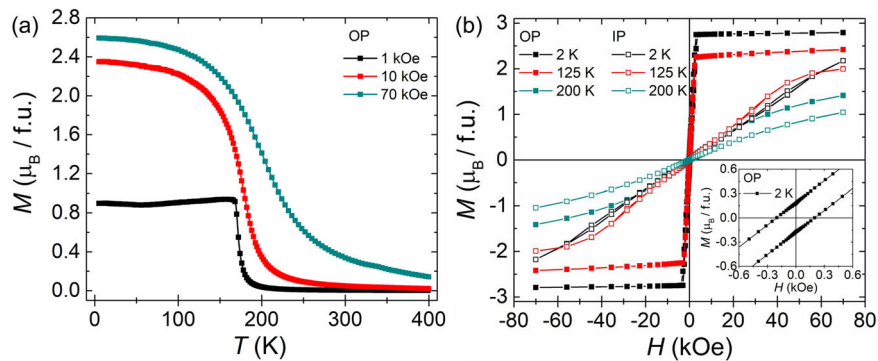


Fig. 2 Magnetic characterization of a $\text{Cr}_{1+\delta}\text{Te}_2$ bulk crystal. **a** Temperature (T) dependence of magnetization (M) of $\text{Cr}_{1+\delta}\text{Te}_2$ for several applied magnetic fields (H) oriented along the out-of-plane direction [0001]. **b** Isothermal magnetization versus magnetic field oriented along in-plane (IP) and out-of-plane (OP) directions of the single crystalline platelet sample at 2, 125 and 200 K. Inset of **b** shows the magnified $M(H)$ profile at 2 K for the OP direction.

approximately 200 Oe at 2 K. In addition, temperature dependent XMCD measurements (Fig. S7 in SI) confirm the existence of a finite magnetic remanence (XMCD signal at $H = 0$ up to 200 K), indicating a long-range nature of the magnetic ordering.

Since the inversion symmetry is broken in $\text{Cr}_{1+\delta}\text{Te}_2$, a DMI is possible so that chiral non-collinear spin textures can form. In addition, magnetotransport measurements (see Fig. S12 in SI) reveal clear evidence for a topological Hall effect that is indicative of a non-trivial topological magnetic texture. In order to investigate the magnetic textures in $\text{Cr}_{1+\delta}\text{Te}_2$ we carried out temperature- and field-dependent magnetic imaging experiments using LTEM. Specimens for LTEM studies were prepared in the form of thin [0001] oriented single crystalline $\text{Cr}_{1+\delta}\text{Te}_2$ lamellae using focused ion-beam milling (FIB). The lamella was initially zero-field cooled from 368 to 100 K followed by LTEM imaging. Under this condition a cycloidal state was found as the ground state (see Fig. S13 in SI). With increasing magnetic field the cycloidal state gradually transforms into a field-polarized state without stabilizing any skyrmion state. A skyrmion state was stabilized after field-cooling the lamella from 368 to 100 K in the presence of a magnetic field of 320 Oe that was oriented perpendicular to the lamella, i.e. parallel to the easy axis of $\text{Cr}_{1+\delta}\text{Te}_2$. The magnetic field was then set to zero and LTEM images were recorded in an under-focus condition ($\Delta f = -1.5$ mm). No magnetic contrast is observed when the electron beam is oriented parallel to the lamella [0001] direction, as shown in Fig. 3b. However, a magnetic contrast becomes visible once the lamella is tilted a few degrees away from the impinging electron beam (see schematic in Fig. 3a). Data for a tilt angle of 15° (around the y -axis, here denoted as $+\alpha$ tilt) are shown in Fig. 3c. The LTEM image shows small circular features that are characterized by dark and bright contrast at their opposite edges. This contrast is reversed for opposite tilt angles ($-\alpha$ tilt, see Fig. 3d). Similarly, for a tilt about the x -axis ($\pm\beta$ tilt), the magnetic contrast is rotated by 90° relative to the $\pm\alpha$ -tilt (see Fig. 3e, f). These observations are characteristic features of Néel-type skyrmions. In the absence of sample tilting the in-plane components of the magnetic texture are aligned either radially outward or inward. Therefore, the deflected incoming electrons do not generate any intensity modulation in the defocused image plane resulting in the absence of any magnetic contrast³⁷. Tilt angle-dependent LTEM images of these Néel skyrmions are shown in the SI (see Fig. S14). Figure 3g shows a LTEM image collected at a lower defocus condition ($\Delta f = -0.5$ mm), where we see a similar magnetic contrast as for $\Delta f = -1.5$ mm, showing that the contrast is characteristic of the spin texture in this range of defocus values of 0.5–1.5 mm. Figure 3h shows the calculated LTEM contrast for two opposite tilt angles of a prototypical Néel-type skyrmion-bubble, as discussed in methods²⁶, demonstrating that the objects we observe are clearly Néel-type.

From the XRD analysis it is concluded that the symmetry of the crystal structure corresponds to the C_{3v} point group which fulfills the symmetry requirements for hosting Néel-type magnetic textures³⁸. The LTEM images indicate that the magnetic nanostructure consists of a larger uniformly magnetized core along with a narrow Néel-wall at its periphery. Furthermore, the magnetic nanostructures in our $\text{Cr}_{1+\delta}\text{Te}_2$ sample do not form a well-ordered hexagonal 2D lattice. For these reasons we propose that the magnetic textures are not only stabilized by the DMI but are also affected by long-range dipole-dipole interactions (DDI)³⁹ and can therefore be considered as Néel skyrmion bubbles. The DDI is also known to stabilize skyrmionic bubbles (type-I; typically, Bloch-like)⁴⁰ and topologically trivial bubbles (type-II)⁴¹. Both of these textures are characterized by an almost uniformly magnetized center-part and a narrow circular domain wall, which surrounds the inner part. Type I and type II bubbles have the same out-of-plane profile and only differ in the in-plane orientation of the magnetic moments. Upon increasing the magnetic field the uniformly magnetized center part that is magnetized opposite to the applied field shrinks, while the domain wall width remains roughly the same.

In the following, the stability and size-dependence of the Néel skyrmions under variation of the magnetic field and thickness of the lamella is described. At first, we show the results of the magnetic field-induced evolution of the spin textures after field cooling at a field of 320 Oe applied along the [01 $\bar{1}$ 1] direction. Similar results are found for fields in the range of 60–320 Oe. At lower fields the skyrmions are intermixed with cycloidal structures and at higher fields the skyrmion density is lower. Since the magnetic contrast is bigger, the larger is the tilt angle, we show the LTEM images of skyrmions with the electron beam directed along the [0111] direction under different magnetic fields at 100 K (Fig. 4), corresponding to a tilt angle of $\approx 33^\circ$ with respect to the sample normal [0001]. The initial state in the presence of the field shows the presence of Néel skyrmions as shown in Fig. 4a. Upon reducing the magnetic field to zero the skyrmions remain stable (Fig. 4b), while their average size becomes larger by $\approx 8\%$. Further increase of the magnetic field up to 640 Oe (Fig. 4d) leads to a decrease of the density of skyrmions until they start to disappear when the field strength is increased from 960 to 1280 Oe (Fig. 4e–g). Finally, at 1600 Oe almost the whole lamella is in the field-polarized state together with just a few isolated skyrmions (Fig. 4h).

The field-driven evolution of the skyrmions is studied for two different thickness regions [≈ 75 nm and ≈ 162 nm labeled as region I (bright) and region II (dark), respectively]. Following the field-cooling from 368 K in a vertical magnetic field of 64 Oe oriented parallel to the [0001] direction, Néel skyrmions were stabilized in both thickness regions (Fig. 5a, b). The skyrmions

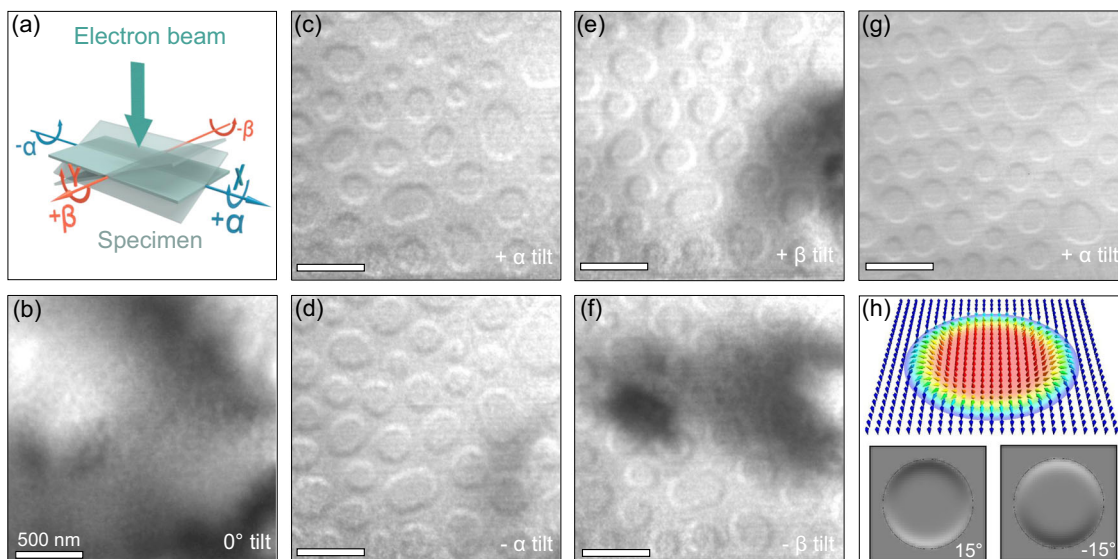


Fig. 3 Néel-type magnetic textures in a thin lamella of $\text{Cr}_{1+\delta}\text{Te}_2$ at 100 K. **a** Definition of tilt angles, α and β , that are defined with respect to the [0001] direction. When $\alpha = \beta = 0$, the electron beam of the transmission electron microscope is transmitted along [0001]. **b** Lorentz transmission electron microscopy (LTEM) image under zero tilt. **c–f** LTEM images in zero magnetic field for **(c–d)** $\alpha = \pm 15^\circ$ and **(e–f)** $\beta = \pm 15^\circ$. All images are recorded at a defocus value of -1.5 nm. The large darkened areas correspond to bending contours. The lamella has a thickness of ≈ 82 nm. All micrographs are obtained from the same region. **g** LTEM image at a defocus value of -0.5 nm in zero magnetic field upon $+4^\circ$ tilting from the [0111] direction that corresponds to $\alpha = +33^\circ$, showing that the magnetic contrast is similar to that obtained at a higher defocus value. The lamella has a thickness of ≈ 75 nm. **h** Calculated LTEM contrast of the Néel skyrmion for a tilt of $\pm 15^\circ$ about the vertical axis in the image.

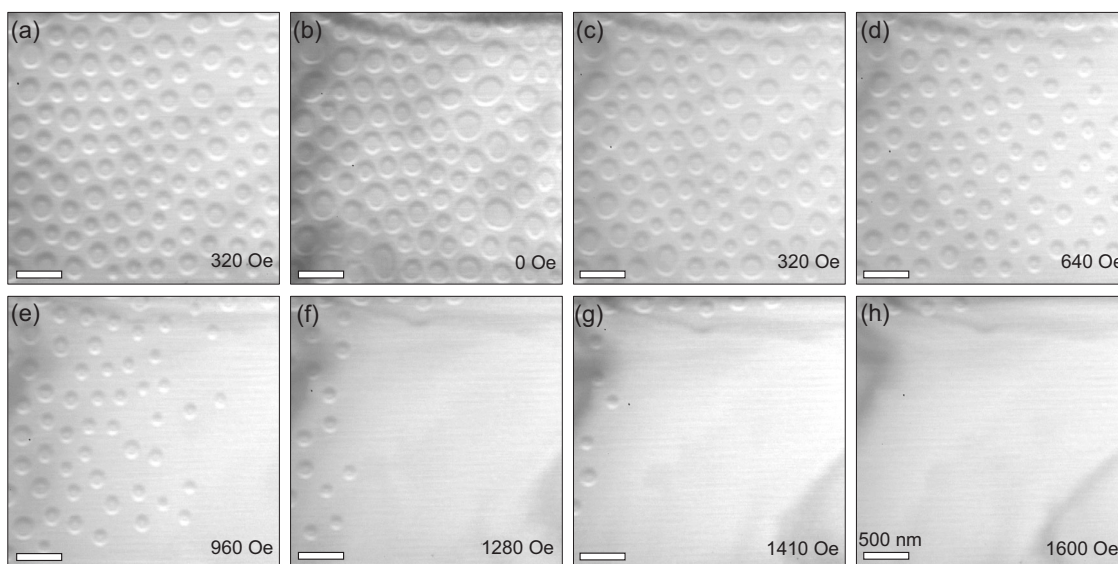


Fig. 4 Evolution of Néel-type textures in a thin lamella of $\text{Cr}_{1+\delta}\text{Te}_2$ as a function of magnetic field at 100 K. **a–h** Lorentz transmission electron microscopy images of Néel-type textures collected at different magnetic fields by tilting the lamella 7° away from the [0111] direction. These images are acquired at a defocus value of -1.2 nm. The lamella has a thickness of ≈ 75 nm.

are larger in region II than in region I. With increasing magnetic field, skyrmions first disappear at 1280 Oe from region I, while they are still stable within region II, i.e. the skyrmions are considerably more stable within the thicker region until, at a field strength beyond 2048 Oe, all skyrmions have completely been transformed into the field-polarized state. Although in both regions the magnetic objects appear simultaneously under the same magnetic field, their disappearance at a different magnetic field points to a significant thickness dependence of their stability window. In general, the diameter of skyrmions decreases with increasing field. The relation between skyrmion diameter and applied field within both regions is shown in Fig. 5c. An

interesting point is that the width of the size distribution at a given field decreases as the field is increased. This is consistent with the role of DDI mentioned earlier. As the central core region shrinks with increasing field, the size of the skyrmions is determined largely by the Néel domain wall width and the influence of the DDI becomes less important. It is clear that the broad size distribution in small fields is governed by DDI rather than by any intrinsic variation of the magnetic properties. LTEM images recorded at temperatures varying from 100–220 K are shown in SI (see Fig. S15). We note that there is no significant temperature-dependence of the skyrmion diameter for this temperature range, as shown in Fig. 5d. This would imply that the magnetization is

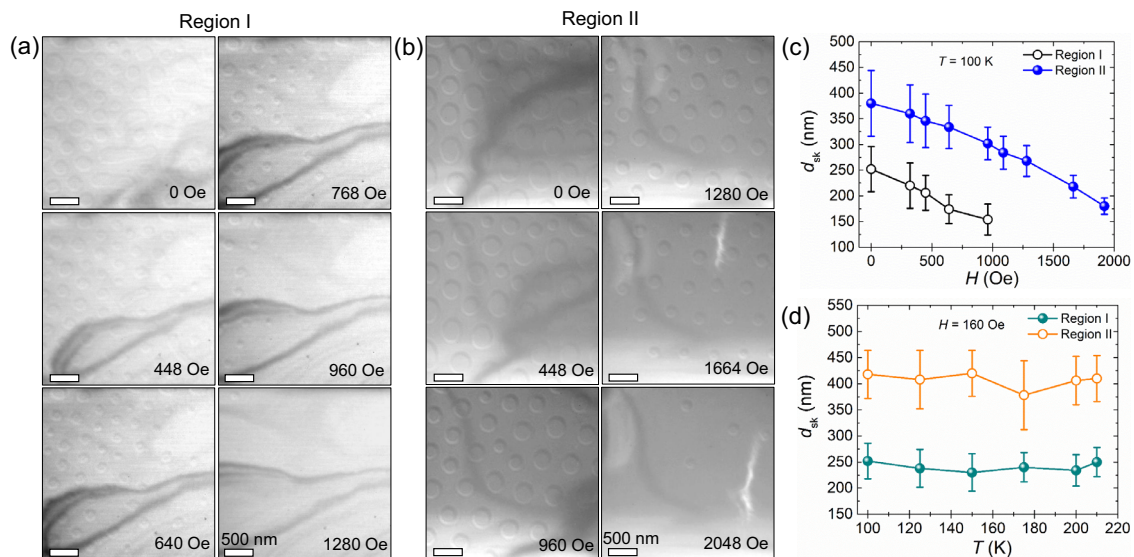


Fig. 5 Thickness-dependent evolution of Néel-type textures in a thin lamella of $\text{Cr}_{1+\delta}\text{Te}_2$ as a function of magnetic field at 100 K. **a, b** Lorentz transmission electron microscopy image of Néel-type textures recorded at different magnetic fields for $\alpha = +6^\circ$ for lamella thicknesses of **a** ≈ 75 nm (Region I) and **b** ≈ 162 nm (Region II). These images are acquired at a defocus value of -1.5 nm. **c** Skyrmion diameter (d_{sk}) versus magnetic field (H) for Regions I and II. **d** Skyrmion diameter (d_{sk}) versus temperature (T) for Regions I and II. The dark lines correspond to bending contours. The error bars in **c, d** represent the standard deviation in the skyrmion diameter.

also insensitive to temperature in this range otherwise, as discussed in Ref. 26, the DDI would evolve with temperature. Interestingly, as shown in Fig. 2a, the magnetization for low fields, where we observe the skyrmions, is nearly independent of temperature up to close to the Curie temperature.

In summary, we have found a new crystal structure for the self-intercalated vdW compound $\text{Cr}_{1+\delta}\text{Te}_2$ ($\delta \approx 0.3$) which is characterized by the presence of two symmetry inequivalent vdW gaps per unit cell. This structure lacks inversion symmetry which is thereby compatible with the presence of bulk DMI which makes possible the presence of the Néel-type skyrmions that we observe below the Curie temperature of ≈ 200 K. The properties of these Néel spin textures are similar to those reported in PtMnGa ³⁸ and Fe_3GeTe_2 ⁴² which have crystal structures with the same SGR. We also note that the significant role of DDI is similar to that found in the inverse tetragonal Heusler compounds although these compounds, which have a different SGR, rather host anti-skyrmions and elliptical Bloch skyrmions²⁶. Our results provide an example that in vdW materials self-intercalation can generate very complex atomic geometries in otherwise simple crystal structures which opens up new perspectives to create vdW crystals by tuning self-intercalation with novel functionalities.

Methods

Structural and magnetic characterization. The X-ray diffraction experiments were carried out using a Gallium Jet X-ray source operated at an acceleration voltage of 70 kV and a power of 200 W emitting Ga- K_α radiation ($\lambda = 1.341$ Å) monochromatized by a Montel optics. The intensities of the diffracted peaks were collected with a six-circle diffractometer and a two-dimensional Pilatus 100k pixel detector. Temperature dependent experiments were carried out in a helium cooled Cryovac Konti Micro cryostat. Integrated intensities of the diffraction peaks used for the structure analysis were collected by transverse (theta-) scans which were subsequently subject to instrumental correction factors (Lorentz-, polarization, effective area, absorption) to derive the structure factor magnitudes. The temperature and field (H) dependent magnetization (M) measurements of the single crystal of $\text{Cr}_{1+\delta}\text{Te}_2$ ($\delta \approx 0.3$) were carried out with a SQUID-VSM [MPMS3, Quantum design].

Transmission electron microscopy. For the transmission electron microscopy (TEM) investigations, several lamellae from the same single crystal of $\text{Cr}_{1+\delta}\text{Te}_2$ were prepared by Focused Ion Beam (FIB) Ga^+ ion milling [TESCAN GAIA3 operating at 30 kV ion-beam energy] using standard lift-out procedures. Final polishing of the lamellae was performed with lower Ga^+ ion-beam energies (5 kV) to reduce the

thickness of any amorphous surface layers. The thickness, t , of the lamella was measured using Energy Filtered TEM (EFTEM) by the log-ratio method from the relationship, $t = \lambda \ln(I_t/I_0)$, where λ is the total inelastic mean free path of the electrons, and I_t and I_0 are the total and zero-loss intensities in the EELS spectrum, respectively⁴³. The error in measuring t is $\sim 10\%$. Magnetic textures were investigated by TEM [FEI TITAN 80-300] in the Lorentz mode operated at an accelerating voltage of 300 kV using a GATAN double-tilt sample holder which is capable of varying the temperature between 100 and 368 K. A vertical magnetic field was applied to the lamella within the TEM column by passing currents through the coils of the objective lens and a Lorentz mini-lens was used for imaging.

Calculation of Lorentz TEM image contrast. We have calculated the Lorentz TEM images based on the method in Ref. 26. The density of transmitted electrons determines the contrast at position (x, y) as

$$I(x, y) = \int \exp\left[-\frac{(x - d \cdot m_y(x', y') - x')^2 + (y + d \cdot m_x(x', y') - y')^2}{a^2}\right] dx' dy'$$

The electron beams are approximated as Gaussian functions with a smearing factor $a = 1$ nm. Due to the Lorentz force, the averaged magnetization $m(r)$ along the layers leads to a transverse deflection of the incoming electron beams. The maximum deflection is controlled by $d = 0.5$ nm.

Data availability

The data that support the findings of this study are available from the corresponding author upon request.

Code availability

The source code for the calculations performed in this work is available from the corresponding authors upon request.

Received: 14 November 2021; Accepted: 14 June 2022;

Published online: 08 July 2022

References

- Novoselov, K., Mishchenko, O. A., Carvalho, O. A. & Neto, A. C. 2D materials and van der Waals heterostructures. *Science* **353**, aac9439 (2016).
- Gong, C. & Zhang, X. Two-dimensional magnetic crystals and emergent heterostructure devices. *Science* **363**, eaav4450 (2019).
- Parkin, S. S. P. & Friend, R. 3d transition-metal intercalates of the niobium and tantalum dichalcogenides. I. Magnetic properties. *Philos. Mag. B* **41**, 65 (1980).
- Parkin, S. S. P., Marseglia, E. & Brown, P. Magnetic structure of $\text{Co}_{1/3}\text{NbS}_2$ and $\text{Co}_{1/3}\text{TaS}_2$. *J. Phys. C: Solid State Phys.* **16**, 2765 (1983).

5. Du, K. et al. Topological spin/structure couplings in layered chiral magnet $\text{Cr}_{1/3}\text{TaS}_2$: The discovery of spiral magnetic superstructure. *Proc. Natl. Acad. Sci.* **118**, e2023337118 (2021).
6. Zhao, X. et al. Engineering covalently bonded 2D layered materials by self-intercalation. *Nature* **581**, 171 (2020).
7. Burch, K. S., Mandrus, D. & Park, J.-G. Magnetism in two-dimensional van der Waals materials. *Nature* **563**, 47 (2018).
8. Gong, C. et al. Discovery of intrinsic ferromagnetism in two-dimensional van der Waals crystals. *Nature* **546**, 265 (2017).
9. Huang, B. et al. Layer-dependent ferromagnetism in a van der Waals crystal down to the monolayer limit. *Nature* **546**, 270 (2017).
10. Bedoya-Pinto, A. et al. Intrinsic 2D-XY ferromagnetism in a van der Waals monolayer. *Science* **374**, 616 (2021).
11. O'Hara, D. J. et al. Room temperature intrinsic ferromagnetism in epitaxial manganese selenide films in the monolayer limit. *Nano Lett.* **18**, 3125 (2018).
12. Freitas, D. C. et al. Ferromagnetism in layered metastable 1T-CrTe₂. *J. Phys. Condens. Matter* **27**, 176002 (2015).
13. Meng, L. et al. Anomalous thickness dependence of Curie temperature in air-stable two-dimensional ferromagnetic 1T-CrTe₂ grown by chemical vapor deposition. *Nat. Commun.* **12**, 809 (2021).
14. Zhang, X. et al. Room-temperature intrinsic ferromagnetism in epitaxial CrTe₂ ultrathin films. *Nat. Commun.* **12**, 2492 (2021).
15. Sun, X. et al. Room temperature ferromagnetism in ultra-thin van der Waals crystals of 1T-CrTe₂. *Nano Res.* **13**, 3358 (2020).
16. Fujisawa, Y. et al. Tailoring magnetism in self-intercalated $\text{Cr}_{1+\delta}\text{Te}_2$ epitaxial films. *Phys. Rev. Mater.* **4**, 114001 (2020).
17. Huang, M. et al. Significant perpendicular magnetic anisotropy in room-temperature layered ferromagnet of Cr-intercalated CrTe₂. *2D Mater.* **8**, 031003 (2021).
18. Purbawati, A. et al. In-plane magnetic domains and Néel-like domain walls in thin flakes of the room temperature CrTe₂ van der Waals ferromagnet. *ACS Appl. Mater. Interfaces* **12**, 30702 (2020).
19. Nye, J. F. *Physical properties of crystals: their representation by tensors and matrices.* (Oxford university press, 1985).
20. Dzyaloshinsky, I. A thermodynamic theory of "weak" ferromagnetism of antiferromagnetics. *J. Phys. Chem. Solids* **4**, 241 (1958).
21. Moriya, T. Anisotropic superexchange interaction and weak ferromagnetism. *Phys. Rev.* **120**, 91 (1960).
22. Bogdanov, A. N. & Yablonskii, D. A. Thermodynamically stable "vortices" in magnetically ordered crystals. The mixed state of magnets. *Zh. Eksp. Teor. Fiz.* **95**, 182 (1989).
23. Nagaosa, N. & Tokura, Y. Topological properties and dynamics of magnetic skyrmions. *Nat. Nanotechnol.* **8**, 899 (2013).
24. Nayak, A. K. et al. Magnetic antiskyrmions above room temperature in tetragonal Heusler materials. *Nature* **548**, 561 (2017).
25. Kézsmárki, I. et al. Néel-type skyrmion lattice with confined orientation in the polar magnetic semiconductor GaV₄S₈. *Nat. Mater.* **14**, 1116 (2015).
26. Jena, J. et al. Elliptical Bloch skyrmion chiral twins in an antiskyrmion system. *Nat. Commun.* **11**, 1115 (2020).
27. Saha, R. et al. Intrinsic stability of magnetic anti-skyrmions in the tetragonal inverse Heusler compound $\text{Mn}_{1.4}\text{Pt}_{0.9}\text{Pd}_{0.1}\text{Sn}$. *Nat. Commun.* **10**, 5305 (2019).
28. Polyakov, A. et al. Fermi surface chirality induced in a TaSe₂ monosheet formed by a Ta/Bi₂Se₃ interface reaction. *Nat. Commun.* **13**, 2472 (2020).
29. Yang, M. et al. Creation of skyrmions in van der Waals ferromagnet Fe₃GeTe₂ on (Co/Pd)_n superlattice. *Sci. Adv.* **6**, eabb5157 (2020).
30. Wu, Y. et al. Néel-type skyrmion in WTe₂/Fe₃GeTe₂ van der Waals heterostructure. *Nat. Commun.* **11**, 3860 (2020).
31. The crystal was prepared by the 2D Semiconductors Company, Scottsdale, AZ 85251, USA. <https://www.2dsemiconductors.com/2d-semiconductors>.
32. Hatakeyama, K., Kaneko, T., Yoshida, H., Ohta, S. & Anzai, S. Pressure effect on the Curie temperatures of Cr_{1-δ}Te compounds. *J. Magn. Magn. Mater.* **90**, 175 (1990).
33. Hahn, T., Shmueli, U. & Arthur, J. W. *International tables for crystallography.* (Reidel Dordrecht, 1983).
34. Abrahams, S. Indicators of accuracy in structure factor measurement. *Acta Crystallogr. Sect. A: Cryst. Phys., Diffr., Theor. Gen. Crystallogr.* **25**, 165 (1969).
35. The unweighted residuum (Ru) is defined by: $Ru = \frac{\sum_{\text{HKL}} |F_{\text{obs}}(\text{HKL}) - |F_{\text{calc}}(\text{HKL})||}{\sum_{\text{HKL}} |F_{\text{obs}}(\text{HKL})|}$, where F_{obs} and F_{calc} are the experimental and calculated structure factors, respectively and the summation extends over all reflections (HKL). Buerger, M. J. *Contemporary Crystallography*, McGraw-Hill Book Company (New York, 1970).
36. Figueroa, A. et al. Magnetic Cr doping of Bi₂Se₃: evidence for divalent Cr from x-ray spectroscopy. *Phys. Rev. B* **90**, 134402 (2014).
37. McVitie, S. et al. A transmission electron microscope study of Néel skyrmion magnetic textures in multilayer thin film systems with large interfacial chiral interaction. *Sci. Rep.* **8**, 5703 (2018).
38. Srivastava, A. K. et al. Observation of robust Néel skyrmions in metallic PtMnGa. *Adv. Mater.* **32**, 1904327 (2020).
39. Ma, T. et al. Tunable magnetic antiskyrmion size and helical period from nanometers to micrometers in a D_{2d} Heusler compound. *Adv. Mater.* **32**, 2002043 (2020).
40. Yu, X. Z. et al. Magnetic stripes and skyrmions with helicity reversals. *PNAS* **109**, 8856 (2012).
41. Loudon, J. C. et al. Do images of Biskyrmions show type-II bubbles? *Adv. Mater.* **31**, 1806598 (2019).
42. Chakraborty, A. et al. Magnetic Skyrmions in a thickness tunable 2D ferromagnet from a defect driven Dzyaloshinskii-Moriya interaction. *Adv. Mater.* **34**, 2108637 (2022).
43. Malis, T., Cheng, S. & Egerton, R. EELS log-ratio technique for specimen-thickness measurement in the TEM. *Microsc. Res. Tech.* **8**, 193 (1988).

Acknowledgements

We would like to acknowledge the funding by the Deutsche Forschungsgemeinschaft (DFG, German Research Foundation)—SPP 2137 (project number - 403505322) and SPP 2244 (project number - 443406107). B.G. and I.M. acknowledge support from the DFG under SFB TRR 227. A.B.-P. acknowledges CELLS-ALBA for the allocation of synchrotron radiation beamtime under proposal 2020094576-2 and thanks P. Gargiani and M. Valdivares for assistance with the XMCD experiments, performed at BOREAS beamline with the collaboration of ALBA staff and CALIPSOplus (Grant 730 872) funding. A.B.-P. acknowledges support by the Generalitat Valenciana (CIDEAGENT/2021/005). A.E. acknowledge the funding by the Fonds zur Förderung der Wissenschaftlichen Forschung (FWF) under grant I 5384. Calculations were carried out at the Rechenzentrum Garching of the Max-Planck Society.

Author contributions

R.S. and S.S.P.P. conceived of the study. R.S. performed the Lorentz TEM experiments and analyzed the images with input from H.D. R.S. and B.K.H. carried out the magnetic characterization and magnetotransport measurements. H.L.M. carried out X-ray diffraction and analyzed the data together with K.M. B.G. carried out image simulation under the supervision of I.M. A.B.-P. performed XMCD measurements. V.A. and A.E. carried out first principles calculations. D.K. prepared TEM lamellae. R.S., H.L.M., and S.S.P.P. wrote the manuscript. All authors discussed the data and commented on the manuscript. S.S.P.P. supervised the project.

Funding

Open Access funding enabled and organized by Projekt DEAL.

Competing interests

The authors declare no competing interests.

Additional information

Supplementary information The online version contains supplementary material available at <https://doi.org/10.1038/s41467-022-31319-y>.

Correspondence and requests for materials should be addressed to Stuart S. P. Parkin.

Peer review information *Nature Communications* thanks Gan Wang, Jun Woo Choi and the other, anonymous, reviewer(s) for their contribution to the peer review of this work.

Reprints and permission information is available at <http://www.nature.com/reprints>

Publisher's note Springer Nature remains neutral with regard to jurisdictional claims in published maps and institutional affiliations.



Open Access This article is licensed under a Creative Commons Attribution 4.0 International License, which permits use, sharing,

adaptation, distribution and reproduction in any medium or format, as long as you give appropriate credit to the original author(s) and the source, provide a link to the Creative Commons license, and indicate if changes were made. The images or other third party material in this article are included in the article's Creative Commons license, unless indicated otherwise in a credit line to the material. If material is not included in the article's Creative Commons license and your intended use is not permitted by statutory regulation or exceeds the permitted use, you will need to obtain permission directly from the copyright holder. To view a copy of this license, visit <http://creativecommons.org/licenses/by/4.0/>.

© The Author(s) 2022